Surface Reconstruction for Planning and Navigation of Liver Resections

Rafael Palomar[a,b,*], Faouzi A. Cheikh[a], Bjørn Edwin[b], Azeddine Beghdadhi[c], Ole J. Elle[b,d]

[a]*Norwegia Media Technology Lab, Faculty of ComputerScience and Media Technology, NTNU, Teknologivegen 22, 2815 Gjøvik, Norway.*
[b]*The Intervention Centre, Oslo University Hospital, P.O. box 4950 - Nydalen, 0424 Oslo, Norway.*
[c]*L2TI, Institut Galilée, Université Paris 13, Avenue J. B. Clément 99, 93430 Villetaneuse, France.*
[d]*Department of Informatics, University of Oslo, 0373 Oslo, Norway.*
[e]*Faculty of Medicine, University of Oslo, 0372, Oslo, Norway.*

Abstract

Computer-assisted systems for planning and navigation of liver resection procedures rely on the use of patient-specific 3D geometric models obtained from computed tomography. In this work, we propose the application of Poisson surface reconstruction (PSR) to obtain 3D models of the liver surface with applications to planning and navigation of liver surgery. In order to apply PSR, the introduction of an efficient transformation of the segmentation data, based on computation of gradient fields, is proposed. One of the advantages of PSR is that it requires only one control parameter, allowing the process to be fully automatic once the optimal value is estimated. Validation of our results is performed via comparison with 3D models obtained by *state-of-art* Marching Cubes incorporating Laplacian smoothing and decimation (MCSD). Our results show that PSR provides smooth liver models with better accuracy/complexity trade-off than those obtained by MCSD. After estimating the optimal parameter, automatic reconstruction of liver surfaces using PSR is achieved keeping similar processing time as MCSD. Models from this automatic approach show an average reduction of 79.59% of the polygons compared to the MCSD models presenting similar smoothness properties. Concerning visual quality, on one hand, and despite this reduction in polygons, clinicians perceive the quality of automatic PSR models to be the same as complex

*Corresponding author
Email address: rafael.palomar@hig.no (Rafael Palomar)

MCSD models. On the other hand, clinicians perceive a significant improvement on visual quality for automatic PSR models compared to optimal (obtained in terms of accuracy/complexity) MCSD models. The median reconstruction error using automatic PSR was as low as 1.03 ± 0.23 *mm*, which makes the method suitable for clinical applications. Automatic PSR is currently employed at Oslo University Hospital to obtain patient-specific liver models in selected patients undergoing laparoscopic liver resection.

Keywords: Surface Modeling, Planning, Navigation, Liver Resection, Visualization, Reconstruction, Poisson, Marching Cubes.

---

1. Introduction

Liver cancer is the second most common cause of cancer death worldwide [1]. Hepatocellular carcinoma (**HCC**), which accounts for 70% to 80% of the cases [2], presents a 5-year survival rate below 12% [3]. Colorectal cancer metastatic to the liver, on the other hand, develops in 50% of the cases of colorectal cancer, and presents 5-year survival rates up to 58% for selected patients undergoing liver resection [4].

Liver resection is the treatment of choice for patients with localized HCC [5] and can potentially be a curative therapy. A successful surgical resection requires the complete removal of the tumoral cells including a safety margin, preserving as much healthy tissue as possible [6]. Resections with adequate tumor-free margins lead to a better prognosis [7].

For more than a decade, computer-assisted surgical systems have been helping surgeons and other clinicians in the decision making process for planning and guiding surgical interventions. In the case of liver resection, these systems have recently found their way into the clinical practice, providing different patient-specific models: geometric, mechanical and functional as well as simulations. These models, ultimately rely on pre-operative computed tomography (**CT**) or magnetic resonance imaging (**MRI**).

The use of patient-specific 3D geometric models improve the capacity of surgeons to understand the liver and the underlying vascular structures. Using three-dimensional (**3D**) reconstructions have shown not only improvements in tumor localization and pre-

cision of surgery planning [8, 9, 10], but also an improved orientation and confidence of the surgeon while operating[11].

Marescaux *et al.* [12] were the first in implementing a system for planning and visualization applied to liver resection. In their approach, 3D models of the liver surface and vessels (tumors were artificially introduced) were built from MRI. The 3D models, based on simplex meshes [13], could be manipulated for visualization and allowed deformations for simulation purposes. Later, Selle *et al.* [14] introduced the analysis of the hepatic vascular structures, which enabled the identification of the liver segments.

More recent approaches allowed the definition of a virtual resection as well as new visualization techniques. Reitinger *et al.* [15] presented a virtual reality environment in which the planning was performed by direct manipulation of 3D structures. Lamata *et al.* [16] also introduced a progressive clipping visualization based on the advancement of resection during surgery. Hansen *et al.* [17] encoded distance to critical structures in the surface representing the virtual resection.

Most of the visualization systems for planning and navigation of liver resection interventions, including all the aforementioned works, rely on the construction of 3D geometric models. These models have traditionally been obtained by isosurface extraction from segmented anatomical structures (parenchyma and venous vasculature) and tumors. Three-dimensional modeling of liver vasculature has been widely studied in the scientific literature [18, 19, 20, 21, 22, 23], however, very little attention has been given to the modeling of parenchyma and tumors.

Marching cubes (**MC**) is the most widespread technique to obtain 3D models of anatomical structures in the liver. The method was originally developed by Lorensen and Cline [24] as an isosurface extraction method from scalar volumetric data. A number of extensions to the original MC have been proposed along the scientific literature [25]. MC provides with accurate isosurfaces which strictly adheres to the underlying data. In the context of isosurface extraction from medical images, MC leads to surfaces with a high number of polygons and vertices, and the appearance of *staircase* artifacts. Different mechanisms like mesh smoothing [26, 27, 28] and decimation [29] have been employed to palliate these effects at the expense of adding more processing stages and control parameters.

Poisson surface reconstruction (**PSR**), originally proposed by Kazdhan *et al.* [30], is a 3D surface reconstruction technique which works on dense clouds of oriented points. In the literature, PSR finds application in reconstructions where clouds of points are inherent to the acquisition (scanning) technology. Examples of such applications can be reconstruction of scenes using structured light sensors [31], laser scanners [32] and stereo cameras [33]. The noise resilience of PSR makes it a remarkable method for coping with the inherent noise acquired by these technologies. In the medical imaging context, PSR has found very little application perhaps due to the fact that, in this domain, the input data consist of 3D scalar fields rather than oriented cloud of points. In order to apply PSR to medical images, Leonardi *et al.* [34] performed an estimation of the oriented clouds of points by fitting a plane to a segmented surface point and its *k-nearest* neighbors. Other approaches like [35] propose an extension to PSR to perform adaptive polygonization with application to vessel modeling.

1.1. Major Contributions

The goal of this work is to address two common problems in 3D modeling techniques in the context of surgery planning and navigation. On one hand, integration of medical imaging, segmentation and 3D modeling methods into clinical workflows requires an elevated degree of automation. As an alternative to automation, expert users can perform manual adjustments of the reconstruction parameters. On the other hand, models employed in planning and navigation are increasingly becoming more complex, both in terms of resolution and dimensionality of the underlying data. Processing these models is very demanding in terms of computing power, especially with the introduction of real-time constraints.

To overcome these problems and with the aim of facilitating the integration of 3D modeling techniques in clinical workflows, we propose the application of PSR as a technique to model the liver surface (parenchyma). In order to adapt the segmented images to clouds of points (as required by PSR), a method based on gradient fields computation is described (Section 2.1).

Unlike traditional analysis of 3D modeling techniques, where different reconstruction parameters are considered separately, we propose a multi-objective optimization

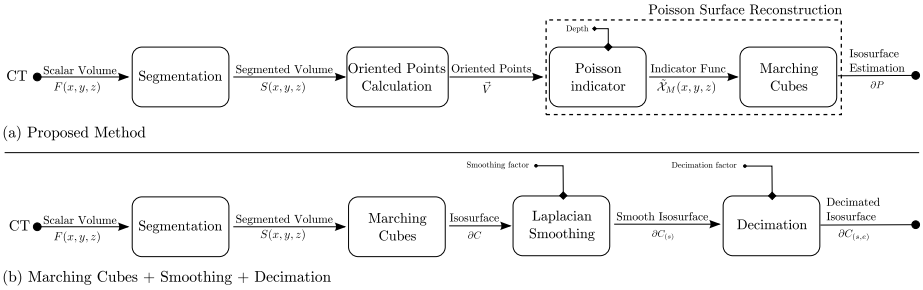

Figure 1: Processing stages for the proposed approach, based on PSR (a) and the *state-of-the-art* MCSD (b).

framework consisting of a bi-dimensional accuracy/complexity optimization space (Section 3) . The aim is to obtain optimal parameters which can lead to automatic 3D model reconstructions.

2. Materials and Methods

The approach presented in this work is used to obtain a 3D geometric model of the liver surface from a segmented volumetric image. Fig. 1 shows the processing stages of both our PSR approach and *state-of-the-art* MCSD.

Isosurface extraction is considered to be an automatic process, however, adding processing stages either after or before, introduces additional parameters which make the process more complicated and thus limiting its applicability and integration into clinical workflows. As opposed to MCSD, our strategy based on PSR requires only one parameter.

In the following, we describe our proposal. We start first by describing the computation of the oriented cloud of points from segmented images. Then we briefly describe the application of PSR to obtain the 3D models of the liver parenchyma.

2.1. Oriented Cloud of Points from Liver Segmentation

As depicted in Fig. 1, medical images, obtained from CT, are represented by the scalar field defined as $F : \mathbb{R}^3 \rightarrow \mathbb{R}$ in which the point $\mathbf{p}_i = (x_i, y_i, z_i)$ with $i = 1, 2, ..., N$ is given a value representing an intensity level $F(\mathbf{p}_i) = v$. Through a segmentation process, the different points of the image, are assigned a class value (label) l_i according

to either anatomical or functional criteria. The segmentation is then defined as a new scalar field $S : \mathbb{R}^3 \rightarrow \{l_1, ..., l_k\}$ with k the number of classes. In our case, since we are only interested in the liver parenchyma, our label map is constrained to the set $\{l_p = 0, l_b = 1\}$ which only considers the classes *parenchyma* and *background*. Fig. 2 shows an example of a scalar volume and its correspondent liver segmentation overlayed.

In order to find the oriented cloud of points $\vec{V} = \{(\mathbf{p}_i, \vec{n}_i)\}$, with $i = 1, 2, ..., N$, where $\vec{n}_i$ are the inward normals at $\mathbf{p}_i$, we exploit two properties of the gradient of the segmented images. On one hand we use the fact that, the gradient of the segmented image, at any point $\mathbf{p}_i$ belonging to the surface of the parenchyma ∂M, is orthonormal to the surface:

$$\nabla S(\mathbf{p}_i) \perp \partial M|_{\mathbf{p}_i} \Leftrightarrow \mathbf{p}_i \in \partial M. \tag{1}$$

On the other hand, the points $\mathbf{p}_i$ laying on the surface ∂M, can be discriminated in terms of the gradient of the segmented image:

$$\mathbf{p}_i \in \partial M \Leftrightarrow \|\nabla S(\mathbf{p}_i)\| > 0. \tag{2}$$

Using the properties established in Eq. 1 and Eq. 2, the definition of a oriented cloud of points $\vec{V}$ can be entirely expressed in terms of the gradient of the binary image:

$$\vec{V} = \{(\mathbf{p}_i, \vec{n}_i)\} = \{\ (\mathbf{p}_i, \nabla S(\mathbf{p}_i))\ \mid\ \|\nabla S(\mathbf{p}_i)\| > 0\ \}, \tag{3}$$

with $i = 1, 2, ..., N$.

In contrast to Leonardi *et al.* [34], in which the authors estimate the normals by local plane fitting of the *k-nearest* neighbors, we propose the obtention of oriented clouds of points through the approximation of the gradient of segmented images. Our implementation obtains the gradient of a 3D binary image through the application of the 3D Sobel operator. This operator approximates the partial derivatives individually through convolution of the segmented parenchyma with kernel functions:

$$\nabla S = \left(\frac{\partial S}{\partial x}, \frac{\partial S}{\partial y}, \frac{\partial S}{\partial z}\right) = \left(\mathcal{K}_x * S, \mathcal{K}_y * S, \mathcal{K}_z * S\right), \tag{4}$$

where $\mathcal{K}_x, \mathcal{K}_y, \mathcal{K}_z \in \mathbb{R}^{3\times3\times3}$ are the third-order tensors representing the 3D Sobel kernel. The discrete nature of the Sobel operator makes that the condition stated in Eq. 2

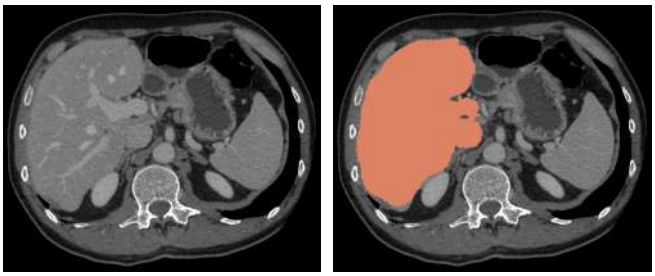

(a) (b)

Figure 2: Slice from CT imaging of the abdomen: (a) scalar field F; (b) segmentation of the parenchyma S overlayed on F.

becomes true for voxels near the surface of the liver (both inside and outside). Therefore, our implementation considers Eq. 3 only for those voxels belonging to the liver, this is, $S(\mathbf{p}_i) = l_p$.

2.2. Poisson Surface Reconstruction

PSR obtains smooth watertight (i.e. absence of holes in the mesh) triangulated approximations of surfaces from oriented cloud of points. The method utilizes a function fitting strategy which brings the benefit of both local and global fitting approaches together. Furthermore, PSR presents high resilience to noise.

Fig. 3 shows the general idea behind PSR. To obtain the surface, PSR uses the oriented cloud of points $\vec{V}$ to reconstruct an indicator function $\mathcal{X}_M : \mathbb{R}^3 \rightarrow \mathbb{R}$ of a parenchyma model M. This indicator function resembles the segmented image S, this is, a function in which the values inside the parenchyma are $l_p = 0$ and the values outside the parenchyma are $l_b = 1$. The oriented cloud of points $\vec{V}$ can be thought of as a set of samples taken from the gradient of the indicator function $\nabla\mathcal{X}_M$. Then the problem can be stated as finding the scalar function $\mathcal{X}_M$ whose gradient best matches the cloud of points $\vec{V}$:

$$\tilde{\mathcal{X}}_M = \arg\min_{\mathcal{X}_M} \|\nabla\mathcal{X}_M - \vec{V}\| \tag{5}$$

with $\|.\|$ the Euclidean norm.

Khazdan *et al.* [30] makes use of the divergence operator to transform this problem into a variational problem optimized by solving the Poisson equation:

$$\Delta\mathcal{X} \equiv \nabla \cdot \nabla\mathcal{X} = \nabla \cdot \vec{V} \tag{6}$$

where $\mathcal{X}$ is an indicator function and $\vec{V}$ is a vector field.

The solution is represented through an adaptive and multi-resolution basis. More precisely, PSR constructs the minimal octree $\mathcal{O}$ with the property that every point sample falls into a leaf node at depth d. Intuitively, one can think of the depth as a parameter controlling the granularity of the mesh. Higher depth values thus lead to more complex models able to represent smaller features (and *vice versa*). Each octree node $o \in \mathcal{O}$ is associated with a function F_o. Bolitho *et al.* [36] proposes to associate a tri-variate B-spline (translated and scaled by the size of the node) to each node of the octree. The span $\mathcal{F}$ of translated and scaled B-splines defines the function space employed to solve the Poisson equation (Eq. 6). The system is solved through a finite elements approach where the system is discretized by using elements F_o as test functions. The solution is given by the function $\tilde{\mathcal{X}} \in \mathcal{F}_{\mathcal{O},F}$ such that:

$$\langle \Delta\tilde{\mathcal{X}}, F_o \rangle = \langle \nabla \cdot \vec{V}, F_o \rangle \mid \forall o \in \mathcal{O} \tag{7}$$

Finally, in order to obtain the surface approximation ∂P, isosurface extraction is applied to the average value of $\tilde{\mathcal{X}}$ at the sample positions:

$$\partial P \equiv \{\mathbf{q} \in \mathbb{R}^3 \mid \tilde{\mathcal{X}}(\mathbf{q}) = \gamma\} \text{ with } \gamma = \frac{1}{N} \sum_{(\mathbf{p}_i, \vec{n}_i) \in \vec{V}} \tilde{\mathcal{X}}(\mathbf{p}) \tag{8}$$

Different implementations of PSR have been proposed along the scientific literature. The original approach ([30]) extends the method to the case of non-uniformly distributed cloud of points. PSR it is considered as an efficient method for which parallel implementations have also been proposed [36].

2.3. Experimental Setup

In this work, we propose the application of PSR for planning and navigation of liver resection procedures compared to the *state-of-the-art* MCSD. For comparison

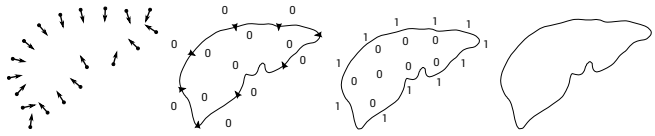

Figure 3: Overview of Poisson surface reconstruction in 2D contour of liver parenchyma: (a) oriented set of points $\vec{V}$; (b) gradient of the indicator function $\nabla\mathcal{X}_M$; (c) indicator function $\mathcal{X}_M$; (d) surface ∂P.

purposes, we employ the implementation (C++) of MCSD included in 3D Slicer [37] in its version 4.4.0.

Our PSR implementation (C++), which incorporates the computation of oriented cloud of points described in 2.1, is based on Doria and Gelas [38], who adapted the original by Kazhdan *et al.*[30].

The experiments are performed on a data set consisting of six CT volumes acquired from the abdomen of patients undergoing liver resection under the Oslo-CoMet study (NCT01516710) [39]. These images were acquired with parameters normally employed for diagnostics and surgical purposes. The images, presenting different image spacing and different liver volumes (Table 1), were segmented (parenchyma, vessels, tumors) by biomedical engineers in a semi-automatic way using ITK-Snap [40] and reviewed by two laparoscopic surgeons. All the data sets present anisotropic image spacing, and therefore, are prone to generate *staircase* artifacts which may be distracting and confusing, since these do not have any anatomical foundation.

3. Evaluation Criteria

In this section, the evaluation criteria to compare the PSR approach described in the Section 2 to MCSD are established. There are different ways to evaluate and compare 3D geometric models, however, in this work, we focus on the desirable properties for planning an navigation of liver resection procedures, this is, accuracy, mesh complexity and smoothness.

Table 1: CT data set used in the evaluation.

Name	**Spacing** (in mm)	**Dimensions**	**Liver Volume** (in cm^3)	**CT Scanner**
P_1	$0.79 \times 0.79 \times 0.62$	$512 \times 512 \times 358$	2,289.25	G
P_2	$0.82 \times 0.82 \times 3.00$	$512 \times 512 \times 153$	2,289.39	S
P_3	$0.76 \times 0.76 \times 0.60$	$512 \times 512 \times 461$	1,853.56	G
P_4	$0.63 \times 0.63 \times 0.62$	$512 \times 512 \times 299$	1,579.10	G
P_5	$0.68 \times 0.68 \times 2.50$	$512 \times 512 \times 179$	1,503.66	G
P_6	$0.70 \times 0.70 \times 0.62$	$512 \times 512 \times 396$	2,326.09	G

G: GE Medical Systems Lightspeed VCT.

S: Siemens Sensation 16.

3.1. Mesh Complexity and Accuracy

Precise planning and navigation of liver resection procedures requires high accuracy of the 3D models. Some works like Wu *et al.* [23] rely on the Hausdorff distance as a metric for accuracy, however, Hausdorff distance is known to be sensitive to noise, which is inherent to medical images. In the same line as Oeltze and Preim [18] and Schumann *et al.*[19], we approximate the 3D reconstruction accuracy using surface distance based metrics, particularly the *point-to-surface* distance $\bar{\delta}(\partial M)$ has been employed. This distance is computed from all points $\mathbf{p}_i$ in a reference cloud of points $\vec{V}$ to all the points $\mathbf{q}$ in the model ∂M (either obtained by PSR or MCSD):

$$\bar{\delta}(\partial M) = \frac{1}{L} \sum_{i=1}^{L} \min_{\mathbf{q} \in \partial M} \|\mathbf{p}_i - \mathbf{q}\| \ , \ \mathbf{p}_i \in \vec{V}, \tag{9}$$

where L is the number of points in ∂M.

In mesh modeling, mesh complexity and accuracy are variables related to each other. Decreasing the mesh complexity generally leads to a decreased accuracy (and *vice versa*). Therefore, obtaining an acceptable trade-off between complexity and accuracy can then be established in terms of a multi-objective optimization problem (i.e. obtaining low complexity and high accuracy).

Number of polygons and mean *point-to-surface* distance are expressed in different

units on different scales. To bring them into a unit-less objective space on the same scale, linear normalization is applied (Fig. 4), thus obtaining the normalized mean *point-to-surface* distance $\hat{\bar{\delta}} \in [0, 1]$ and the normalized number of polygons $\hat{N} \in [0, 1]$:

$$\begin{cases} \hat{\bar{\delta}}(\partial M) = \dfrac{\bar{\bar{\delta}}(\partial M) - \bar{\bar{\delta}}_{min}}{\bar{\bar{\delta}}_{max} - \bar{\bar{\delta}}_{min}} \\ \hat{N}(\partial M) = \dfrac{N - N_{min}}{N_{max} - N_{min}} \end{cases} , \tag{10}$$

where N is the number of points in ∂M, and $\bar{\bar{\delta}}_{min}$, $\bar{\bar{\delta}}_{max}$, N_{min} and N_{max} refer to the extreme values, considering all models (including MCSD and PSR) for a given parenchyma M.

By using normalization, it is established that both objectives are equally important and so, the optimal reconstruction is obtained by minimizing the objective score σ defined as:

$$\sigma(\partial M) = \sqrt{\hat{\bar{\delta}}^2(\partial M) + \hat{N}^2(\partial M)} \, . \tag{11}$$

Models presenting a score value closer to 0, exhibit better trade-off between accuracy and complexity. Then, the best model among all PSR models ∂P_{best}, the best model among all MCSD models ∂C_{best} and the absolute best model ∂M_{best} can be computed as follows:

$$\begin{cases} \partial P_{best} = \arg\min\limits_{\partial P} \sigma(\partial P) \, , \; \partial P \in \mathcal{P} \\ \partial C_{best} = \arg\min\limits_{\partial C} \sigma(\partial C) \, , \; \partial C \in \mathcal{C} \\ \partial M_{best} = \arg\min\limits_{\partial M} \sigma(\partial M) \, , \; \partial M \in \mathcal{P} \cup \mathcal{C} \end{cases} , \tag{12}$$

where $\mathcal{P}$ and $\mathcal{C}$ are the sets of all PSR and MCSD respectively, for a given parenchyma.

3.2. Mesh Smoothness

Liver parenchyma is inherently a smooth organ. Smoothness in the 3D model is essential for visualization since it contributes to the natural appearance of the organ.

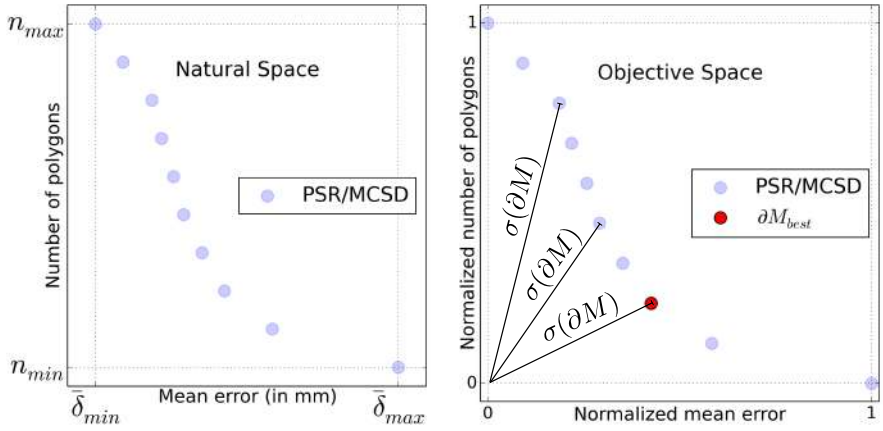

(a) (b)

Figure 4: Normalization and objective score. (a) PSR and MCSD models represented in natural space; (b) PSR and MCSD in objective space where the scores $\sigma_{\partial M}$ are used to compute the best model (∂M_{best}) in terms of accuracy and complexity.

Evaluation of the smoothness is performed through the discrete mean Gaussian curvature as a metric of the roughness of the model ∂M:

$$\bar{K}(\partial M) = \frac{1}{N}\sum_{i=1}^{N}\frac{3(2\pi - \sum_j \gamma_j)}{A(\mathbf{p}_i)}\ ,\ \mathbf{p}_i \in \partial M, \tag{13}$$

where γ_j denote the angles between pairs of edges converging at $\mathbf{p}_i$ and $A(\mathbf{p}_i)$ is the sum of the areas of triangles having $\mathbf{p}_i$ as vertex. Values of the mean Gaussian curvature closer to 0 are then interpreted as smoother appearance of the model.

Despite the fact that other curvature metrics (e.g. mean curvature) are available [41], gaussian curvature seems to be the most widespread in comparisons similar to the one presented in this work [42, 21, 23].

For further comparisons in terms of accuracy and complexity, it will be useful to consider also the MCSD models ∂C_{sim} which present the most similar smoothness to the best PSR models ∂P_{best}. These models ∂C_{sim} can be computed as:

$$\partial C_{sim} = \arg\min_{\partial C} |\bar{K}(\partial C) - \bar{K}(\partial P_{best})|\ ,\ \partial C \in C. \tag{14}$$

3.3. Processing Time

3D models supporting planning and navigation of liver resection procedures are computed *pre-operatively* (i.e. before the operation) and therefore, there is no need to attend to real-time constraints. However, it is desirable that new methods involved in surgery planning and navigation, do not alter the clinical workflow significantly in a negative way.

Medical image processing is often performed in terms of a *region of interest* **ROI**, which represents a reduced set of the original data. In general, this greatly improves the performance of algorithms in terms of processing time, since the number of elements to process decreases dramatically. Therefore, the evaluation of the performance (processing time) presented in this work is performed in the basis of minimal ROIs containing the liver.

3.4. Visual Quality

Perceived visual quality of the 3D models is an important evaluation criterion since it can affect not only the interpretation of the anatomy of the patient but also the confort of the clinicians working with the 3D models. In the scientific literature, visual quality is often discussed in terms of appearance of artifacts in the model and smoothness properties [19, 21, 22, 23].

Some works explicitly introduce visual quality criteria in the evaluation, like in Oeltze *et al.* [18] for 3D modeling or Feng *et al.* [43] for 3D visualization in laparoscopic surgery.

In the same line, we introduce subjective evaluation of visual quality based on the opinion of experts. In our experiment, we recruited 8 laparoscopic liver surgeons ([7-30] years of experience). Each expert is asked the following question: *"Evaluate the quality of the virtual models (parenchyma) for their use in resection planning and surgery guidance"*. In order to evaluate the quality of the 18 liver parenchyma models a 5-levels Likert scale was employed: *Very low* (1), *Low* (2), *Medium* (3), *High* (4), *Very high* (5). The evaluated parenchyma models correspond to the ∂P_{best}, ∂C_{best} and ∂C_{sim} models generated from the dataset described in Table 1. To ensure completeness of visualization, parenchyma models are shown together with vessels and tumors obtained

by application of MCSD under the same parameters chosen arbitrarily. The experts were enforced to evaluate the quality of the parenchyma regardless of the quality of vessels and tumors. The evaluation was performed in a desktop computer (19 inches screen at 1600x1200@60Hz), similarly to typical surgery planning stations.

In order to control possible biases, we followed the guidelines presented in [44]. Remarkable question design aspects taking into account are specificity of question (not allowing ambiguities or misinterpretations), simplicity and use of familiar words as well as clarity of correspondence between numeric values and qualitative tags in the answer fields. The models were presented in random order to avoid patterns in sequential visualizations.

4. Results

4.1. Mesh Complexity and Accuracy

PSR was applied to the 6 liver parenchyma of the data set. A total of 24 surface models were obtained considering PSR at depths $d \in \{5, 6, 7, 8\}$. Fig 5 shows the impact of this parameter on the reconstructions. On one hand, increasing the depth values, also increases the complexity of the model in number of polygons. On the other hand, increasing the depth values also increases the accuracy of the model. At depth $d = 5$, the median error of the 6 data sets is within the range 3.69 ± 0.59 *mm* while the absolute maximum (excluding outliers) is 8.75 *mm*; for $d = 6$, the median error decreases to 1.89 ± 0.34 *mm* with absolute maximum of 4.58 *mm*; for $d = 7$ we obtained a median error as low as 1.03 ± 0.23 *mm* with absolute maximum of 2.79 *mm*; and finally, for $d = 8$ the median error is within the range 0.82 ± 0.36 *mm* with a maximum error of 3.04 *mm*. As it is shown in Fig 5, the most prominent errors are located in areas presenting high curvature and concavities. For low depth values (coarser reconstructions), natural formation of concavities and prominent salients form areas of concentration of high errors. However, as the depth d increases (finer reconstructions), errors not only diminish in magnitude, but also distribute uniformly throughout the organ rather than concentrating in any particular areas.

MCSD presents a more complex parameter space than PSR. To represent the extent of this parameter space we obtained the 50 MCSD models $\partial M_{(s,e)}$ resulting from the combination of $s = \{0, 22, 45, 67, 90\}$ and $e = \{0, 0.1, 0.2, ..., 0.9\}$.

From the application of Eq. 12, the objective score value for all PSR and MCSD models was computed. The results, presented in Table 2, show that PSR with $d = 7$ always present the absolute best score values among all PSR and MCSD models, and therefore better behavior in terms of complexity and accuracy. PSR reconstructions different from $d = 7$ present lower score values than those of the best MCSD.

Table 2: Objective score σ computed for all PSR and best MCSD models.

Parenchyma	**PSR**				**Best**
	$d = 5$	$d = 6$	$d = 7$	$d = 8$	**MCSD**
P_1	1.000	0.416	**0.184**	0.405	0.228
P_2	1.000	0.341	**0.248**	0.541	0.257
P_3	1.000	0.404	**0.165**	0.439	0.226
P_4	1.000	0.418	**0.161**	0.461	0.210
P_5	1.000	0.416	**0.152**	0.312	0.199
P_6	1.000	0.379	**0.148**	0.406	0.205

Minimum objective score highlighted in boldface.

Another interesting comparison concerning accuracy and mesh complexity can be derived from the best MCSD (∂C_{best}), the best PSR models (∂P_{best}) and those MCSD models similar smoothness to ∂P_{best} (Eq. 14). The results reveal that the main contribution to the trade-off difference for ∂C_{sim} is the high number of polygons (460.1 K polygons average) compared to ∂P_{best} (72.4 K polygons average). The relative difference of mean error is low in the comparison of ∂C_{sim} (0.81 *mm* average), ∂P_{best} (1.16 *mm* average) and ∂C_{best} (1.02 *mm* average). Fig. 6 illustrates the compared models derived from P_1.

A broader view of the evaluation results is presented in Fig. 7. In this figure, the performance of all PSR and MCSD are shown in terms of complexity and accuracy. We computed the Pareto frontier, this is, the set of models which are not dominated by

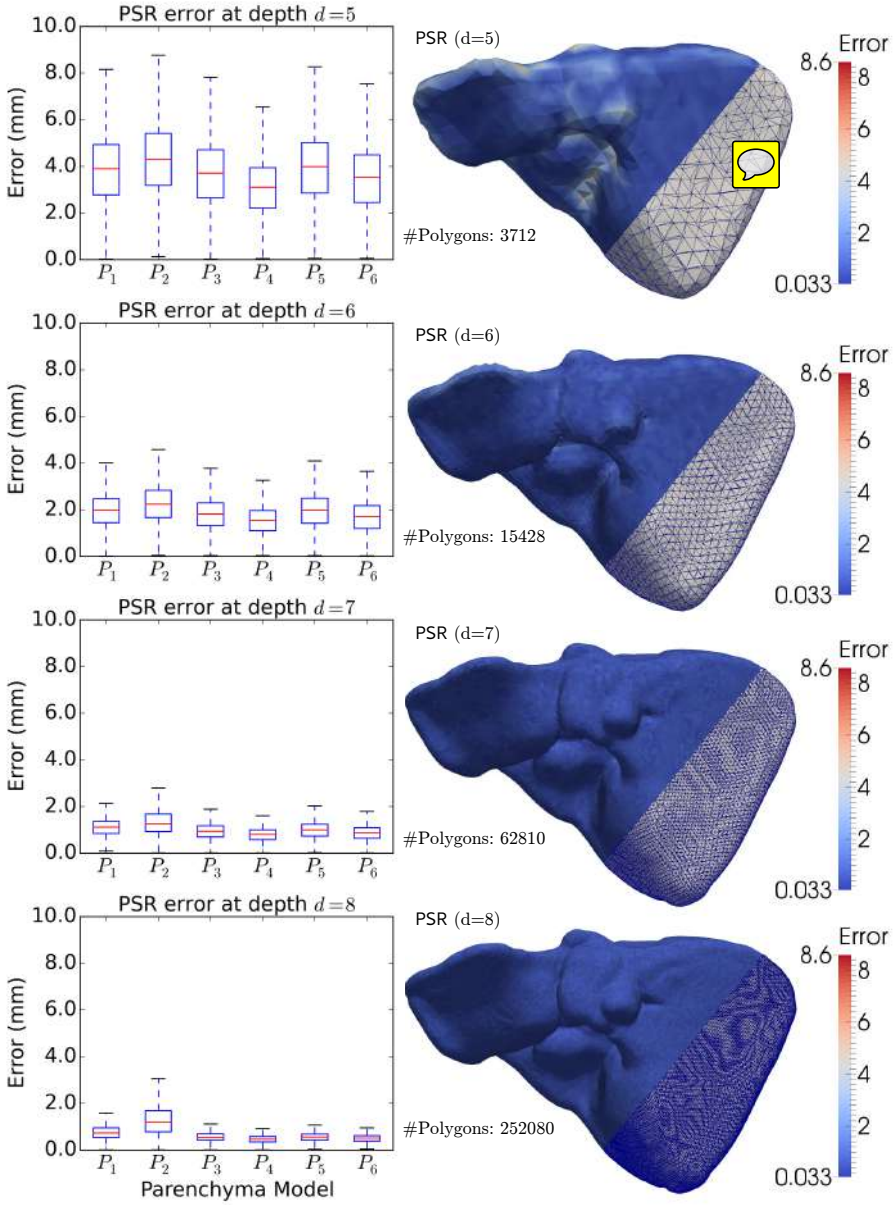

Figure 5: Box plot showing PSR error distribution for depths $d \in \{5, 6, 7, 8\}$ (left). PSR for P_1 at $d \in \{5, 6, 7, 8\}$ including density of polygons and color-coded projection of reconstruction error onto the parenchyma(right).

Table 3: Number of polygons, mean error and objective score σ for best PSR ∂P_{best} (accuracy/complexity), their most similar MCSD ∂C_{sim} (smoothness) and the best MCSD ∂C_{best} (accuracy/complexity).

Parenchyma	P_1			P_2			P_3		
Model	I	II	III	I	II	III	I	II	III
Polygons (in K)	**62**	625	125	75	207	**59**	**71**	263	131
Mean Error	1.11	**0.64**	0.98	**1.37**	1.48	1.79	0.94	**0.81**	0.89
Objective score	**0.18**	1.00	0.22	**0.24**	0.70	0.25	**0.16**	0.40	0.22
Parenchyma	P_4			P_5			P_6		
Model	I	II	III	I	II	III	I	II	III
Polygons (in K)	82	293	**73**	**68**	715	89	74	655	**72**
Mean Error	0.84	**0.72**	1.05	0.99	**0.61**	1.13	0.88	**0.58**	1.11
Objective score	**0.16**	0.40	0.21	**0.15**	0.79	0.19	**0.14**	0.89	0.20

(I) Best PSR ∂P_{best} — (II) Most similar MCSD ∂C_{sim} — (III) Best MCSD ∂C_{best}

Minimum values highlighted in boldface.

any other model in terms of both better accuracy and complexity. For a given model lying in the Pareto frontier, no other model can improve the two objectives, only one or none of the two. The results in Fig. 7 show that all PSR models ∂P, together with some MCSD, including the best MCSD ∂C_{best} models are part of the Pareto frontier. None of the most similar MCSD ∂C_{sim} are part of the Pareto frontier.

4.2. Mesh Smoothness

In order to evaluate the smoothness of the models, the mean Gaussian curvature $\bar{K}$ was computed for all PSR and MCSD models. A comparison of smoothness of PSR models with that of the best MCSD ∂C_{best} and most similar MCSD models ∂C_{sim} in terms of accuracy and complexity was performed. The results, presented in Table 4, show that, on one hand, the best MCSD ∂C_{best} generally presents much higher curvature values than most of PSR and the most similar MCSD ∂C_{sim}. On the other hand, the most similar MCSD ∂C_{sim} (9.67×10^{-3} average curvature) are can only produce

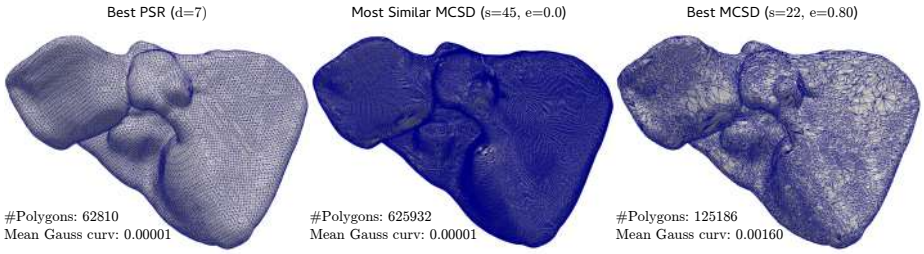

Figure 6: Mesh models correspondent to the best MCSD (accuracy/complexity), best PSR (accuracy/complexity) and its most similar MCSD (smoothness) derived from P_1.

Table 4: Mean Gaussian Curvature $\bar{K}$, excluding outliers ([5-95] percentiles), computed for all PSR ∂P, best MCSD ∂C_{best} and most similar MCSD ∂C_{sim}.

Name	**PSR**				**Similar**	**Best**
	$d = 5$	$d = 6$	$d = 7$	$d = 8$	**MCSD**	**MCSD**
P_1	4.56	0.29	0.19	0.19	0.19	1.60
P_2	11.17	31.96	0.706	14.34	0.72	6186.43
P_3	37.19	52.42	28.28	0.75	17.56	21743.83
P_4	8.22	14.86	151.16	3.15	77.46	20474.71
P_5	2.06	3.27	0.68	0.36	0.68	18494.12
P_6	7.61	5.78	0.32	0.20	0.32	681.94

All values expressed in a scale $\times 10^{-3}$.

relatively less smoothness as their correspondent best PSR ∂P_{best} (0.03×10^{-3} average curvature).

4.3. Processing time

Our performance results (shown in Table 5) were obtained using a CPU Intel® Core™ i7-930 at 2.80GHz. The results were obtained on a basis of *best time of three* executions per model, considering the ROI containing the liver. For PSR, the execution time includes also the computation of the oriented cloud of points.

Mean execution time values show higher performance for similar MCSD models ∂C_{sim} ($\bar{t}_{\partial C_{sim}} = 12.05s$) over best MCSD models ∂C_{best} ($\bar{t}_{\partial C_{best}} = 14.08s$) and best PSR models ∂P_{best} ($\bar{t}_{\partial P_{best}} = 14.50s$), while variability of execution time is significantly lower for ∂P_{best} models ($s_{\partial C_{best}} = 1.24s$) compared to similar MCSD ∂C_{sim} ($s_{\partial C_{sim}} =$

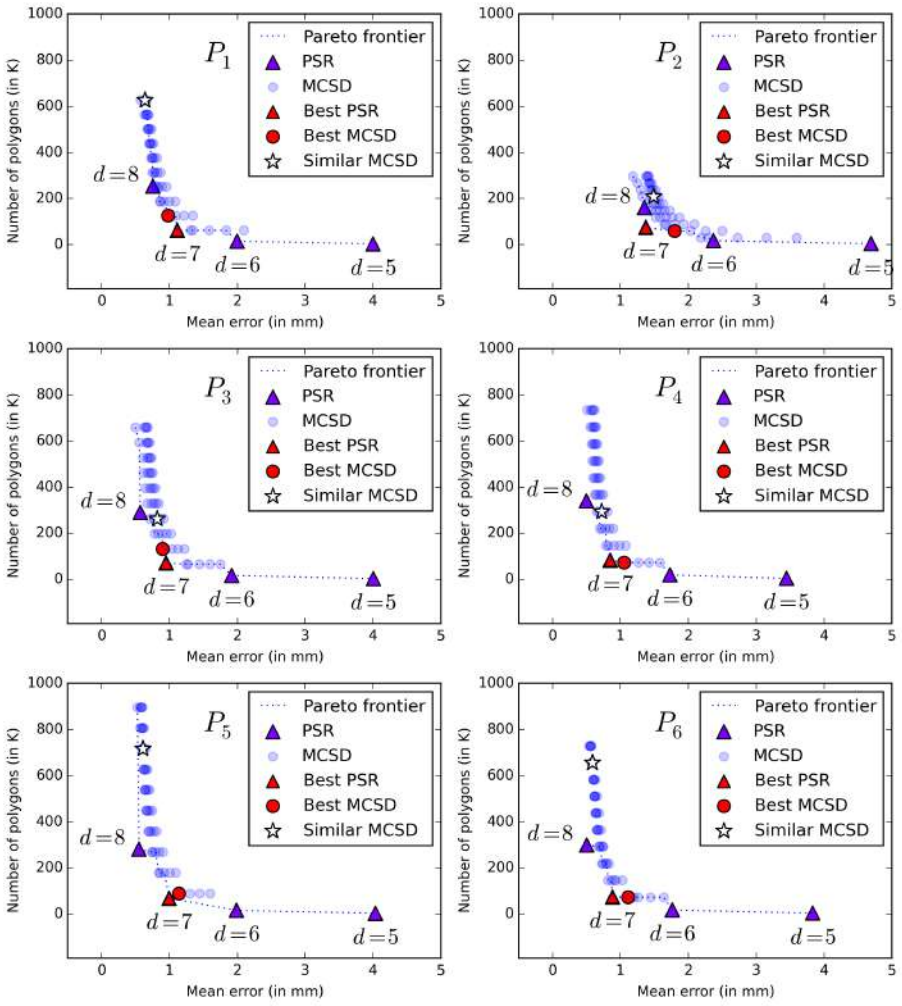

Figure 7: Mesh complexity and accuracy for all MCSD and PSR models derived from the evaluation data set. Best MCSD (complexity/accuracy), together with the best PSR (complexity/accuracy), its most similar MCSD (in smoothness) and the Pareto frontier are highlighted.

Table 5: Processing time (best of three executions, in seconds) the best PSR (including computation of oriented cloud of points) ∂P_{best}, best MCSD ∂C_{best} and most similar MCSD ∂C_{sim}.

Name	Liver Dimensions (Region of Interest)	PSR $d = 7$	Similar MCSD	Best MCSD
P_1	$310 \times 279 \times 330$	14.5	**9.4**	13.7
P_2	$279 \times 286 \times 68$	12.4	**5.8**	6.2
P_3	$296 \times 290 \times 264$	13.8	13.8	**13.0**
P_4	$297 \times 284 \times 272$	15.8	**15.5**	15.7
P_5	$330 \times 345 \times 285$	**15.2**	16.6	19.2
P_6	$280 \times 321 \times 323$	15.3	**11.2**	16.7
	Mean	14.5	**12.05**	14.8
	Std. Dev.	**1.24**	4.06	4.45

Minimum values highlighted in boldface.

4.06s) and best MCSD ∂C_{best} ($s_{\partial C_{best}} = 4.45s$).

4.4. Visual Quality

Subjective data obtained by questionnaires (Fig. 8a) show lower mean quality score for ∂C_{best} ($\bar{s}_{C_{best}} = 2.729$) versus ∂C_{sim} ($\bar{s}_{C_{sim}} = 3.291$) and ∂P_{best} ($\bar{s}_{P_{best}} = 3.333$).

In the same line as Feng *et al.* [43], we test the statistical difference between groups of methods regarding the perceived quality. In our case, the comparison between methods is peformed by means of Welch two sample t-test using the R statistical environment (Fig. 8b). Statistical significance was obtained in the comparison between ∂C_{best} and ∂P_{best} ($p = 0.0006661$), and in the comparison between ∂C_{sim} and ∂C_{best} ($p = 0.001382$). No statistical significance was found in the comparison between ∂P_{best} and ∂C_{sim} ($p = 0.777$).

5. Discussion

5.1. PSR compared to state-of-the-art *MCSD*

The application of PSR to reconstruction of segmented images requires the transformation of the binary image ~~(segmentation)~~ to a cloud of oriented points. Perhaps due

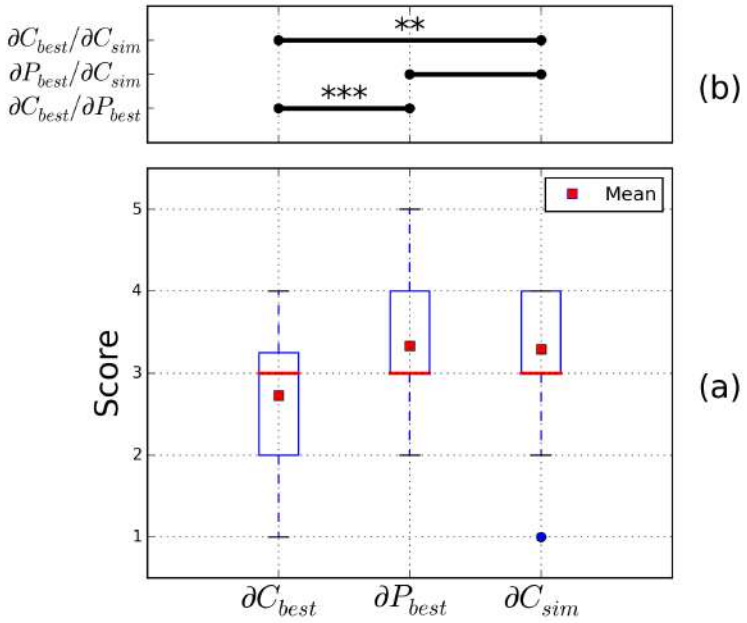

Figure 8: Subjective evaluation results grouped by method (a) and Welch two sample t-test results (b) with ** significant at p = 0.001382 and *** significant at p = 0.0006661.

to this fact, PSR has found very little application in the medical domain. As opposed to Leonardi *et al.* [34], in which PSR is enclosed in a larger method for segmentation and reconstruction, our work focuses on the surface reconstruction process and the comparison of PSR with the *state-of-the-art* MCSD.

The election of PSR as an alternative to be evaluated against *state-of-the-art* MCSD, is justified by the reduced parameter space, the resilience to noise and smoothness properties of PSR. Under the point of view of the application, the reduced parameter space of PSR (not only in number of parameters, but also in possible parameter values), translates into a simpler interaction by clinicians, and hence, a better integration in the clinical workflow. Empirically, we have determined the depth parameter space to be $d \in \{5, 6, 7, 8\}$ in the case of reconstruction of liver parenchyma. This set of values is clearly smaller than all reasonable combinations of smoothing and decimation factors for MCSD. Since the liver is a smooth organ, the good smoothness behaviour exhibited by PSR contributes to the natural appearance of the models. Local features and staircase artifacts are reduced, allowing easier interpretation of the internal structures of the organ (vessels and tumors).

Our results suggest that PSR outperforms *state-of-the-art* MCSD for modeling liver parenchyma in different aspects. Overall, ∂P_{best} present reconstructions with better accuracy/complexity trade-off than *state-of-the-art* MCSD. Comparing models with similar smoothness and visual quality (∂C_{sim} and ∂P_{best}), ∂P_{best} models present a dramatic reduction of complexity (73% less triangles on average) at the cost of decreasing the accuracy slightly. Accuracy values for PSR, however, remain within clinically acceptable limits. Despite ∂C_{best} models can achieve similar complexity as ∂P_{best} in some cases, subjective evaluation experiments reveal that perceived visual quality of ∂C_{best} models is lower with statistical significance than those of ∂P_{best} and ∂C_{sim}.

Based on the accuracy/complexity space (Figure 5) two important observations can be made. First, PSR as method, defines the Pareto frontier, which suggests the goodness of the method over MCSD. Secondly, parameters to obtain ∂C_{best} depend on the input data while PSR obtains ∂P_{best} using the same parameter ($d = 7$), therefore indicating that PSR, as method, is more stable than MCSD. One implication of the stability of PSR is the possibility to perform optimal parameter estimation which can be used to

produce automatic reconstructions (see Section 5.4).

As it is shown earlier in Figure 1, *state-of-art* MCSD requires two parameters (smoothing and decimation factors). In order to integrate automatic MSCD in clinical workflows, a set of values can be established for these parameters. In this line, the possibilities are either ignoring the application of smoothing and decimation, (i.e. considering $s = 0$ and $d = 0$) or choosing a set of "conservative" values that can slightly improve the reconstructions assuming that the optimal is unknown and unreachable. For smooth structures like the liver parenchyma, some degree of smoothing and decimation is beneficial, not only under a polygon-reduction standpoint, but also for visualization purposes. As an alternative to automation, experts (biomedical engineers or clinicians) can manually set the parameters in a *try-and-fail* fashion for every patient. This can be a ~~tediousp~~process and does not guarantee optimality of results.

5.2. PSR Compared to Other Reconstruction Methods

The wide variety of reconstruction techniques in the literature makes the choice of the method a relevant question. The answer to this question is often driven and limited by the scope of the application. There are a number of surface reconstruction methods other than MCSD or PSR. In particular, multi-level partition of unity implicits (**MPUI**) [45] has been previously adopted for vessel modeling from clouds of points [19, 42, 20, 46, 23] and can be applied to liver modeling as well. This and other reconstruction methods are compared and discussed in [30]. In this comparison, MPUI shows generation of spureous surface sheets under noisy conditions, which are inherent in medical imaging, while PSR exhibits good noise resilience.

More recent approaches like dynamic particles [47, 48] provide high-quality meshes suitable for visualization and simulation purposes. These methods show more flexibility (regularity of triangulation and accuracy of reconstructions can be controlled) at the cost of a more complex parameter space. Although these approaches can be better suited for simulation, widening the parameter space complicates the integration into clinical workflows.

5.3. Accuracy, Complexity and Depth Parameter d

The choice of the depth parameter has an impact over the smoothness, accuracy and complexity of the reconstruction. Increasing the depth parameter value generally produces similar or superior smoothness, higher accuracy and higher complexity of the model. Similar works as this study accuracy and complexity as independent dimensions of the problem [19, 42, 21, 23]. For MCSD and PSR, there is a clear relationship between the complexity and accuracy of reconstruction. Low complexity meshes, for instance, present limited representation power for small features, and hence, decreased accuracy.

Considering the accuracy/complexity relationship in a multi-objective optimization framework present some interesting advantages. First, it provides a basis for comparing reconstructions with similar properties: ∂P_{best} vs. ∂C_{best} for optimal accuracy/complexity trade-off and ∂P_{best} vs. ∂C_{sim} for similar smoothness. Secondly, optimal parameters can be estimated. In this line, and by considering accuracy and complexity as equally important objectives (see normalization in Section 4.1), our study suggests that for liver modeling, PSR models with $d = 7$ are optimal in terms of accuracy/complexity trade-off. Other applications might consider different weights for accuracy and complexity objectives, in which case, the optimal depth parameter may vary. In [34], Leonardi *et al.* employ $d = 5$ for kidney modeling attending to a reduction of polygons criterion, however, the authors do not provide any data related to accuracy of reconstruction nor comparison with other methods.

The accuracy/complexity analysis described in this work, can also support automatic generation of multi-resolution PSR models at different d values. Among other purposes, this approach can support the use of proxy geometries for mesh processing and visualization as in [49].

5.4. Integration of PSR in Clinical Workflows

The application domain of our study is planning and navigation of liver resection procedures. In this domain, visual realism and accuracy are of paramount importance. Visual realism is achieved through smoothness, which removes staircase artifacts and

small features not needed for the visualization of the organ, thus reducing the complexity of visualization. Accuracy plays an important role since the model can be used as a base for clinical decisions as well as for *model-to-patient* registration (e.g. surgery navigation). Some of these clinical decisions are supported on operations performed directly on the models. Low complexity models can improve the performance of operations like mesh cutting, mesh volume or distance computations, present in computer-assisted systems for planning and navigation. By optimizing the depth parameter ($d = 7$) we obtained a fully automatic reconstruction method able to produce smooth models with better accuracy/complexity trade-off than the models generated by MCSD. The errors presented in the results for PSR at $d = 7$ (median errors within 1.03 ± 0.23 *mm*) are clinically acceptable. For all this, we consider PSR a suitable candidate to replace *state-of-the-art* MCSD to model 3D for planning and navigation purposes.

The difference in computing time between PSR and MCSD is, for pre-operative purposes, neglectable (Table 5), however, time is still far from real-time reconstructions, which might be of interest for other clinical workflows. The operations involved in PSR are subject to parallelization strategies using graphics processing units (**GPUs**). Works like [31] and [50] show the feasibility of using GPUs for real-time reconstruction of complex scenes using PSR. As intra-operative systems (e.g. surgical navigation) move towards the use of deformable models, aspects related to algorithm performance and parallelization capabilities will get more relevance in medial systems design.

Process automation during imaging, segmentation and 3D modeling is the key for improving the adoption of 3D patient-specific models in clinical workflows. To be sure, the major bottlenkeck is segmentation (currently is subject to extensive research), which automation is still considered as a challenging task [51], thus requiring some degree of human interaction. While segmentation falls out of the scope of this work, the integration ability of PSR and how this can increase the adoption of 3D patient-specific models with the help of *state-of-the-art* tools, like MeVis Distant Services [51, 52, 53] or Fujifilm Synapse VINCENT [54], is a relevant question. PSR can be seamlessly integrated in any medical platform, provided that the platform is able to obtain segmented images (Figure 1). Open source software like 3D Slicer [37] or

ITK-Snap [40] can also make use of this work not only for the reconstruction of liver surfaces, but also to investigate further applications.

Liver surgery is moving towards minimally invasive surgery (laparoscopy). The clinical advantages of this approach must take into consideration the increased complexity of the surgical procedure (reduced maneouvrability and visual field). In this context, the use of 3D patient-specific models, together with intra-operative imaging (ultrasound) are becoming increasingly relevant. Recent studies highlight the advantages of integrating these models as part of augmented reality guidance systems in laparoscopy [55] and open surgery [53]. The combination of 3D patient-specific model, together with the latest trends in surgery, like robotic surgery, have the potential to make surgical interventions easier, faster and probably safer [56]. Some of these works highlight the importance of accuracy, and reduction of human interaction (automation of processes), topics which are widely studied and discussed in this work.

5.5. Application of PSR to Other Anatomical Structures

Our application of PSR to liver modeling (parenchyma) from scalar volumes inevitably raises the question of the adequacy of PSR to obtain 3D models of other anatomical structures. In the context of planning and navigation of liver resection procedures, the question reduces to whether PSR is a suitable method for reconstruction of tumors and vessels.

For tumors, due to their high variability in shape and size, as well as the need of preservation of local features, PSR demands a high d parameter value (associated to a relatively high number of polygons). Though this does not disqualify PSR to be applied to tumors, the advantage of PSR over MCSD is, at the least, not as powerful as for the liver surface. Further investigation is needed to determine the degree of adequacy of PSR for such structures.

In the case of PSR applied to vessels, preservation of high curvature and branches (concavities) demands a high value of the d parameter, resulting in models with high number of polygons. To cope with this problem, Wu *et al.* [23] evaluates a variant of PSR (in that work referred to as *scale-adaptive* [**SA**]), which includes curvature-dependent polygonization (e.g. increasing/decreasing the size of triangles according

to the local curvature) [35]. In [23], other methods including MC (without smoothing and decimation) are evaluated with application to vessel modeling. The authors, point ~~at~~ SA as a suitable method for reconstruction of vessels with applications to surgery planning. The methods evaluated by Wu *et al.* [23] could be also compared with another set of techniques (known as *model-based* methods) [20], widely used in the context of vessel modeling for surgery planning.

5.6. Future Work

Leonardi *et al.* [34] suggest the use of PSR to construct geometric models of other organs than kidney. In the same line, and despite the little attention PSR has been given in the medical domain, we believe that its use can be extended to other organs outperforming *state-of-the-art* methods.

Smooth organs absent of sharp features are, in principle, good candidates to undergo PSR. Evaluations similar to Wu *et al.* [23] could also consider the intrinsic relationship between number of polygons and error according to our multi-objective optimization framework. To the best of our knowledge, modeling of tumors has not been subject to an exhaustive evaluation like the one presented in this work or in Wu *et al.* [23], which can be of great interest.

New reconstruction methods that may arise, can be evaluated using this work as guideline. Despite the more complex parameter space of methods based on dynamic particles [47, 48], these can support an interesting comparison with PSR for modeling of anatomical structures for different purposes.

6. Conclusion

In this work, we propose the application of PSR to obtain patient-specific models of liver parenchyma for planning and navigation of liver resection procedures. For the application of PSR to medical images, we propose an efficient transformation of the segmented images to oriented cloud of points based on computing gradient fields. In order to make an automatic PSR, we found the PSR parameter obtaining the best accuracy/complexity trade-off ($d = 7$).

Comparing PSR with the *state-of-the-art* (MCSD) in terms of accuracy, complexity and smoothness, PSR shows better reconstruction performance and stability of results. This study also reveals that PSR liver models using the optimal parameter $d = 7$ not only are smooth, but also present better accuracy/complexity trade-off than MCSD models. Reconstructions obtained through automatic PSR ($d = 7$), presents median errors within 1.03 ± 0.23 *mm*, which makes them suitable for clinical applications. On average, these models have 79.59% less polygons compared to MCSD models with similar smoothness, while clinicians do not perceive a significant quality difference. Optimal PSR models $d = 7$, exhibit a significant improvement of visual quality compared to optimal MCSD in terms of accuracy/complexity trade-off. Automatic PSR can be seamlessly integrated in clinical workflows already using MCSD, since the processing time is similar to that of MCSD.

The contribution of this work, is therefore, a step towards the automation and quality needed for a wide adoption of 3D patient-specific models in the medical community. Currently, at Oslo University Hospital (The Intervention Centre), PSR is employed in a fully automatic way (after segmentation, which takes place in a semi-automated way) to obtain patient-specific models of liver parenchyma in selected patients undergoing laparoscopic liver resection. Fig. 9a shows a complete patient-specific liver model in which the parenchyma was obtained through PSR ($d = 7$) while MCSD was applied for vessels and tumors. During operation, (Fig 9b) the patient-specific model, which includes the resection path, helps the surgeons to perform the resection according to the pre-operative plan.

[1] A. Jemal, F. Bray, M. M. Center, J. Ferlay, E. Ward, D. Forman, Global cancer statistics., CA: a cancer journal for clinicians 61 (2) (2011) 69–90.

[2] E. Vanni, E. Bugianesi, Obesity and liver cancer., Clinics in liver disease 18 (1) (2014) 191–203.

[3] H. B. El-serag, Hepatocellular Carcinoma, The New England Journal of Medicine 365 (12) (2011) 1118–1127.

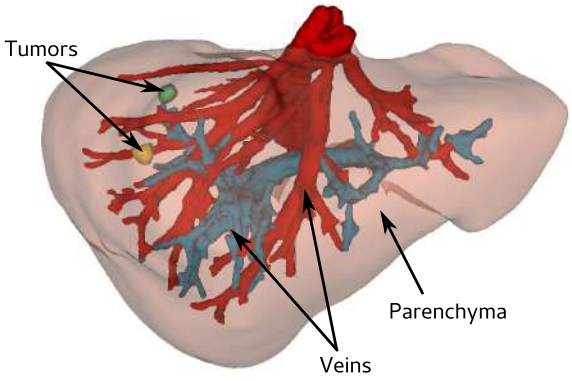

(a)

(b)

Figure 9: (a) Complete patient-specific model including parenchyma (PSR), vessels (MCSD) and tumors (MCSD). (b) Use of a patient-specific model for guiding a liver resection surgical procedure.

[4] E. P. Misiakos, N. P. Karidis, G. Kouraklis, Current treatment for colorectal liver metastases., World journal of gastroenterology : WJG 17 (36) (2011) 4067–75.

[5] R. Bryant, A. Laurent, C. Tayar, J. T. van Nhieu, A. Luciani, D. Cherqui, Liver resection for hepatocellular carcinoma., Surgical oncology clinics of North America 17 (3) (2008) 607–33, ix.

[6] T. M. Pawlik, J.-N. Vauthey, Surgical margins during hepatic surgery for colorectal liver metastases: complete resection not millimeters defines outcome., Annals of surgical oncology 15 (3) (2008) 677–9.

[7] N. Taniai, K. Akimaru, H. Yoshida, T. Tajiri, Surgical treatment for better prognosis of patients with liver metastases from colorectal cancer, Hepatogastroenterology 54 (78) (2007) 1805–1809.

[8] W. Lamadé, G. Glombitza, L. Fischer, P. Chiu, C. E. Cárdenas, M. Thorn, H. P. Meinzer, L. Grenacher, H. Bauer, T. Lehnert, C. Herfarth, The impact of 3-dimensional reconstructions on operation planning in liver surgery., Archives of surgery (Chicago, Ill. : 1960) 135 (11) (2000) 1256–61.

[9] H. Lang, A. Radtke, M. Hindennach, T. Schroeder, N. R. Frühauf, M. Malagó, H. Bourquain, H.-O. Peitgen, K. J. Oldhafer, C. E. Broelsch, Impact of virtual tumor resection and computer-assisted risk analysis on operation planning and intraoperative strategy in major hepatic resection., Archives of surgery (Chicago, Ill. : 1960) 140 (7) (2005) 629–38; discussion 638.

[10] C. Hansen, S. Zidowitz, B. Preim, Impact of model-based risk analysis for liver surgery planning, International Journal of Computer Assisted Radiology and Surgery 9 (3) (2014) 473–80.

[11] P. Lamata, F. Lamata, V. Sojar, P. Makowski, L. Massoptier, S. Casciaro, W. Ali, T. Stüdeli, J. Declerck, O. J. Elle, B. Edwin, Use of the Resection Map system as guidance during hepatectomy., Surgical endoscopy 24 (9) (2010) 2327–37.

[12] J. Marescaux, C. Koehl, Y. Russier, D. Mutter, E. Surgery, G. Epidaure, Virtual Reality Applied to Hepatic Simulation : The Next Revolution, Annals of surgery 228 (5) (1998) 627–634.

[13] H. Delingette, Simplex Meshes : a General Representation for 3D Shape Reconstruction, Tech. rep. (1994).

[14] D. Selle, B. Preim, A. Schenk, H.-O. Peitgen, Analysis of vasculature for liver surgical planning., IEEE transactions on medical imaging 21 (11) (2002) 1344–57.

[15] B. Reitinger, A. Bornik, Liver surgery planning using virtual reality, Computer Graphics and Applications 26 (6) (2006) 36–47.

[16] P. Lamata, a. Jalote-Parmar, F. Lamata, J. Declerck, The Resection Map, a proposal for intraoperative hepatectomy guidance, International Journal of Computer Assisted Radiology and Surgery 3 (3-4) (2008) 299–306.

[17] C. Hansen, S. Zidowitz, F. Ritter, C. Lange, K. Oldhafer, H. K. Hahn, Risk maps for liver surgery., International journal of computer assisted radiology and surgery 8 (3) (2013) 419–28.

[18] S. Oeltze, B. Preim, Visualization of vasculature with convolution surfaces: method, validation and evaluation., IEEE transactions on medical imaging 24 (4) (2005) 540–8.

[19] C. Schumann, S. Oeltze, R. Bade, B. Preim, H. Peitgen, Model-free Surface Visualization of Vascular Trees., in: EuroVis, 2007, pp. 283–290.

[20] B. Preim, S. Oeltze, 3D visualization of vasculature: an overview, 2008.

[21] J. Wu, R. Ma, X. Ma, F. Jia, Q. Hu, Curvature-dependent surface visualization of vascular structures., Computerized medical imaging and graphics : the official journal of the Computerized Medical Imaging Society 34 (8) (2010) 651–8.

[22] Q. Hong, Q. Li, J. Tian, Implicit reconstruction of vasculatures using bivariate piecewise algebraic splines., IEEE transactions on medical imaging 31 (3) (2012) 543–53.

[23] J. Wu, Q. Hu, X. Ma, Comparative study of surface modeling methods for vascular structures., Computerized medical imaging and graphics : the official journal of the Computerized Medical Imaging Society 37 (1) (2013) 4–14.

[24] W. Lorensen, H. Cline, Marching cubes: A high resolution 3D surface construction algorithm, ACM Siggraph Computer Graphics 21 (4) (1987) 163–169.

[25] T. S. Newman, H. Yi, A survey of the marching cubes algorithm, Computers & Graphics 30 (5) (2006) 854–879.

[26] T. Gabriel, T. Zhang, G. Golub, Optimal Surface Smoothing as Filter Design, in: Computer Vision — ECCV '96, Springer Berlin Heidelberg, 1996, pp. 283–292.

[27] R. Bade, J. Haase, B. Preim, Comparison of Fundamental Mesh Smoothing Algorithms for Medical Surface Models., SimVis 1 (c) (2006) 1–16.

[28] T. Moench, S. Adler, B. Preim, Staircase-aware smoothing of medical surface meshes, EG VCBM'10 Proceedings of the 2nd Eurographics conference on Visual Computing for Biology and Medicine.

[29] W. Schroeder, J. Zarge, W. Lorensen, Decimation of triangle meshes, ACM SIGGRAPH 19th annual conference on Computer graphics and interactive techniques 26 (2) (1992) 65–70.

[30] M. Kazhdan, M. Bolitho, Poisson surface reconstruction, Proceedings - Eurographics Symposium on Geometry Processing.

[31] S. Izadi, A. Davison, A. Fitzgibbon, D. Kim, O. Hilliges, D. Molyneaux, R. Newcombe, P. Kohli, J. Shotton, S. Hodges, D. Freeman, Kinect Fusion: Real-time 3D Reconstruction and Interaction Using a Moving Depth Camera, Proceedings of the 24th annual ACM symposium on User interface software and technology - UIST '11 (2011) 559.

[32] R. Sensing, S. I. Sciences, C. Benedek, D. Events, Towards 4D Virtual City Reconstruction From Lidar Point Cloud II (May) (2013) 15–20.

[33] M. Habbecke, L. Kobbelt, A surface-growing approach to multi-view stereo reconstruction, Proceedings of the IEEE Computer Society Conference on Computer Vision and Pattern Recognition.

[34] V. Leonardi, V. Vidal, J. Mari, M. Daniel, 3D reconstruction from CT-scan volume dataset application to kidney modeling, in: Proceedings of the 27th Spring Conference on Computer Graphics, Vol. D, 2011, pp. 111–120.

[35] J. Wu, M. Wei, Y. Li, X. Ma, F. Jia, Q. Hu, Scale-adaptive surface modeling of vascular structures., Biomedical engineering online 9 (1) (2010) 75.

[36] M. Bolitho, M. Kazhdan, R. Burns, H. Hoppe, Parallel poisson surface reconstruction, in: Advances in Visual Computing, Springer, 2009, pp. 678–689.

[37] S. Pieper, M. Halle, R. Kikinis, 3D Slicer, in: 2004 2nd IEEE International Symposium on Biomedical Imaging: Nano to Macro (IEEE Cat No. 04EX821), 2004, pp. 632–635.

[38] D. Doria, A. Gelas, Poisson Surface Reconstruction for VTK, The VTK Journal Januar (2010) 5.

[39] A. A. Fretland, A. M. Kazaryan, B. A. Bjornbeth, K. Flatmark, M. H. Andersen, T. I. Tonnessen, G. M. W. Bjornelv, M. W. Fagerland, R. Kristiansen, K. Oyri, B. Edwin, Open versus laparoscopic liver resection for colorectal liver metastases (the Oslo-CoMet study): study protocol for a randomized controlled trial, Trials 16 (1) (2015) 1–10.

[40] P. a. Yushkevich, J. Piven, H. C. Hazlett, R. G. Smith, S. Ho, J. C. Gee, G. Gerig, User-guided 3D active contour segmentation of anatomical structures: Significantly improved efficiency and reliability, NeuroImage 31 (3) (2006) 1116–1128.

[41] S. Rusinkiewicz, Estimating curvatures and their derivatives on triangle meshes, in: Proceedings - 2nd International Symposium on 3D Data Processing, Visualization, and Transmission. 3DPVT 2004, 2004, pp. 486–493.

[42] C. Schumann, M. Neugebauer, R. Bade, B. Preim, H. O. Peitgen, Implicit vessel surface reconstruction for visualization and CFD simulation, International Journal of Computer Assisted Radiology and Surgery 2 (5) (2008) 275–286.

[43] X. Feng, A. Morandi, M. Boehne, T. Imvised, B. M. Ure, J. F. Kuebler, M. Lacher, 3-Dimensional (3D) laparoscopy improves operating time in small spaces without impact on hemodynamics and psychomental stress parameters of the surgeon, Surgical Endoscopy 29 (5) (2015) 1231–1239.

[44] B. C. Choi, A. W. Pak, for Cdc, A Catalog of Biases in Questionnaires 2 (1) (2005) 1–13.

[45] Y. Ohtake, A. Belyaev, M. Alexa, G. Turk, H.-P. Seidel, Multi-level partition of unity implicits, ACM Transactions on Graphics 22 (3) (2003) 463.

[46] T. Moench, Generation of smooth and accurate surface models for surgical planning and simulation, in: SPIE Medical Imaging 2010: Visualization, Image-Guided Procedures, and Modeling, Vol. 49, 2010.

[47] M. Meyer, R. M. Kirby, R. Whitaker, Topology, accuracy, and quality of isosurface meshes using dynamic particles, IEEE Transactions on Visualization and Computer Graphics 13 (6) (2007) 1704–1711.

[48] M. Meyer, R. Whitaker, R. M. Kirby, C. Ledergerber, H. Pfister, Particle-based sampling and meshing of surfaces in multimaterial volumes, IEEE Transactions on Visualization and Computer Graphics 14 (6) (2008) 1539–1546.

[49] C. Dyken, K. O. Lye, J. Seland, E. W. Bjonnes, J. Hjelmervik, J. O. Nygaard, T. R. Hagen, A framework for OpenGL client-server rendering, in: CloudCom 2012 - Proceedings: 2012 4th IEEE International Conference on Cloud Computing Technology and Science, 2012, pp. 729–734.

[50] K. Zhou, M. Gong, X. Huang, B. Guo, Data-parallel octrees for surface reconstruction, IEEE Transactions on Visualization and Computer Graphics 17 (5) (2011) 669–681.

[51] A. Zygomalas, D. Karavias, D. Koutsouris, I. Maroulis, D. D. Karavias, K. Giokas, V. Megalooikonomou, Computer-assisted liver tumor surgery using a novel semiautomatic and a hybrid semiautomatic segmentation algorithm, Medical and Biological Engineering and Computing.

[52] L. Soler, J. Marescaux, Patient-specific surgical simulation, World Journal of Surgery 32 (2) (2008) 208–212.

[53] S. Nicolau, L. Soler, D. Mutter, J. Marescaux, Augmented reality in laparoscopic surgical oncology, Surgical Oncology 20 (3) (2011) 189–201.

[54] S. Ohshima, Volume analyzer SYNAPSE VINCENT for liver analysis, Journal of Hepato-Biliary-Pancreatic Sciences 21 (4) (2014) 235–238.

[55] D. Ntourakis, R. Memeo, L. Soler, J. Marescaux, D. Mutter, P. Pessaux, Augmented Reality Guidance for the Resection of Missing Colorectal Liver Metastases: An Initial Experience., World journal of surgery 40 (2) (2015) 419–426.

[56] F. Volonté, F. Pugin, P. Bucher, M. Sugimoto, O. Ratib, P. Morel, Augmented reality and image overlay navigation with OsiriX in laparoscopic and robotic surgery: Not only a matter of fashion, Journal of Hepato-Biliary-Pancreatic Sciences 18 (4) (2011) 506–509.